Forschungszentrum Karlsruhe
Technik und Umwelt

Wissenschaftliche Berichte
FZKA 6317

TAILORED POROSITY GRADIENT BY FEM CALCULATIONS FOR SILICON CARBIDE EVAPORATOR TUBES

W. Schaller, Y.Y. Yang, M. Dröschel*

Institut für Materialforschung
*Institut für Keramik im Maschinenbau - Zentrallaboratorium,
Universität Karlsruhe (TH)

Forschungszentrum Karlsruhe GmbH, Karlsruhe
1999

Abstract

Gas turbine combustors with premix burners can reduce NO_x -emissions. In a new premix burner concept the evaporation of the liquid fuel and the burning zone are separated from one another [1].The liquid fuel is sprayed onto the porous outer surface of the evaporator tube. Flowing air and the fuel vapour attain inside the tube where combustion takes place. Previous work has shown that for this application porous silicon carbide (SiC) ceramics show great potential [2] [3]. Due to the temperature gradient during operation, high thermal stresses develop in the tube. Four different design variations for the distribution of the porosity in the outside combustor wall are investigated, which are a two-layer concept (bulk material and a homogeneous porous layer) and three continuous porosity gradients (linear, convex, concave).
By comparing the local stress distribution with the local strength of the four different design variations a favorable porosity gradient is found. Only with this tailored porosity gradient can the failure probability of the component be significant reduced.

Ermittlung eines spannungsreduzierenden Porositätsgradienten für ein Siliziumkarbidverdampferrohr mit Hilfe der Finite Element Methode

Zusammenfassung

Brennkammern mit Vormischbrenner können die NO_x-Emission von Gasturbinen wesentlich reduzieren. In einem neuen Konzept für eine Vormischbrennkammer wird das Verdampfen des flüssigen Brennstoffes und das Verbrennen des Brennstoff-Luftgemisches räumlich getrennt [1]. Der flüssige Brennstoff wird auf die poröse Aussenseite des Verdampferrohres aufgesprüht. Die anströmende Luft und der Brennstoffdampf gelangen in das Verdampferrohr, wo die Verbrennung stattfindet. Vorangegangene Arbeiten zeigten die gute Eignung von Siliziumkarbid für dieses Einsatzgebiet [2] [3].
Bedingt durch den Temperaturgradienten im Betrieb entstehen hohe thermische Spannungen in der Verdampferröhre. Vier verschiedene Designvarianten für den Verlauf der Porosität in der Aussenwand der Brennkammer wurden untersucht: ein Zweischichtsystem (dichtes Material und eine homogen poröse Schicht)und drei kontinuierliche Porositätsgradienten (linear, konvex, konkav).
Durch einen Vergleich der Verläufe von Festigkeiten und Spannungen bei den vier Designvarianten wurde ein geeigneter Verlauf der Porosität gefunden. Mit diesem angepassten Porositätsgradienten kann die Versagenswahrscheinlichkeit des Bauteils wesentlich reduziert werden.

Contents

1 Introduction

A concept for a gas turbine combustor with premix burner is shown in Fig.1. The liquid fuel is sprayed onto the outer diameter of the combustor. Due to the air flowing from the compressor, a thin film of fuel is formed on the outer surface of the evaporator, which vaporizes completely. The homogeneous mixture of air and fuel reaches the reaction zone, where the flame is burning.

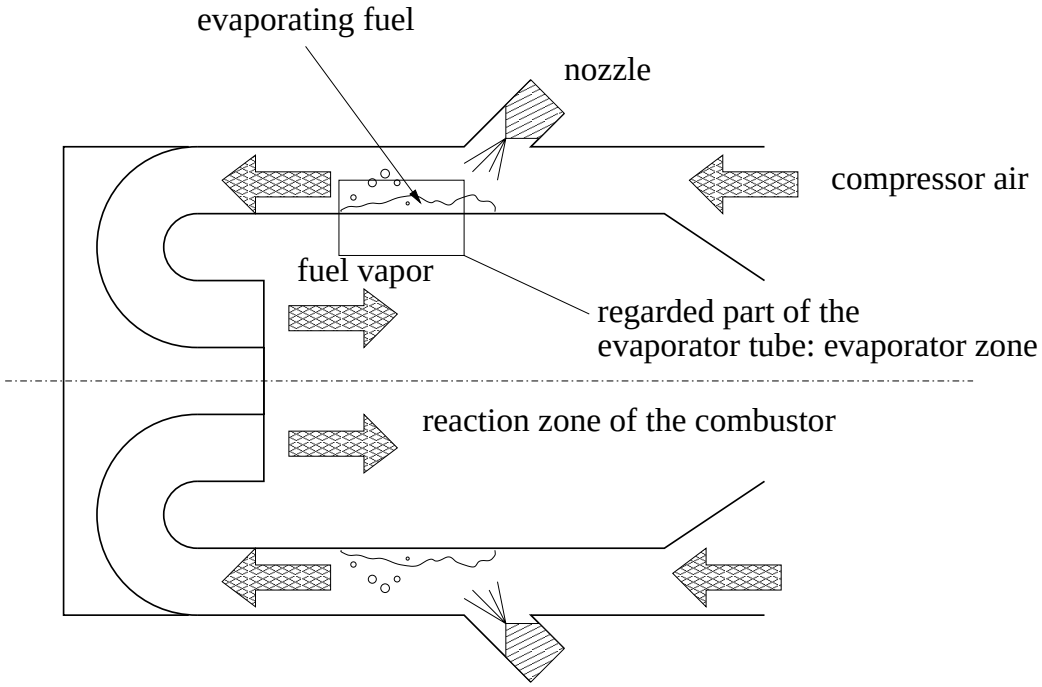

Figure 1: Concept of a gas turbine combustor with premix burner [4].

The evaporizer tube has to be gas-tight on the inside and porous on the outer surface, where the evaporation takes place. The inner side of the tube is heated by the burning fuel, the outer side is cooled by fuel evaporation and compressor air. Due to the temperature gradient between the inner side and the outer side of the tube thermal stresses occure. In order to reduce the thermal stresses and to reach a higher strength of the tube, between this porous outside and the solid inner side a porosity gradient shall be introduced. The present report deals with the design of this porosity gradient. The distribution and value of these stresses are influenced by the porosity gradient, as well as the strength of the porous material. With the help of this porosity gradient an optimum relation between the stresses and strength is attempted to be found.

2 Geometrical boundary conditions

The evaporator tube is simplified as an axial symmetric component with an inner diameter of $r_i = 22.5mm$. The length is assumed to be infinite. The inner side consists of a solid SiC layer with $2mm$ in thickness. This is followed by a porous SiC layer, which is used as an evaporator. Various designs for this porous layer are possible. The first is a homogeneous layer (non-graded) with a thickness of $3mm$ and a constant porosity of 50%. This two-layer joint fulfills, according to former results [3], the request regarding the fuel evaporation. Three alternative porosity gradients are considered, which all posess the porosity of 50% on the outer surface.

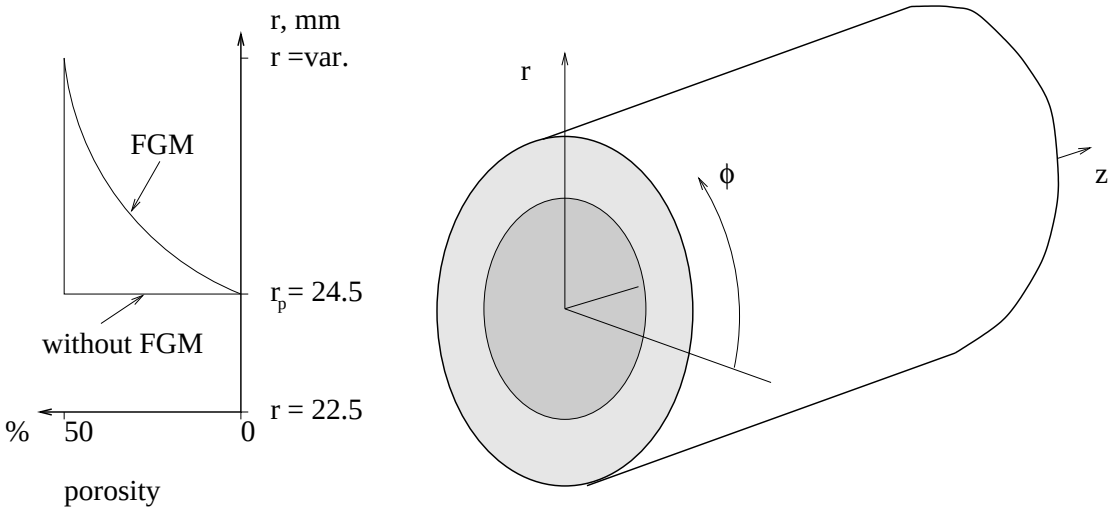

Figure 2: Design of the evaporator tube.

For the gradient case the following function for the porosity p is chosen:

$$P(r) = P(r_a)\left(\frac{r - r_p}{r_a - r_p}\right)^n \quad \text{with} \quad r_p \leq r \leq r_a \quad \text{and} \quad P(r_a) = 50\%, \qquad (1)$$

where r_p is the inner diameter of the porous layer and r_a is the outer diameter of the tube.

With $n = 1$ a linear gradient is obtained, with $n = 0.5$ a convex gradient and with $n = 2.0$ a concave gradient is obtained. The outer diameter r_a of the component

is dependent from an additional boundary condition. To warrant an equivalent evaporation for all four design variants, the flow resistance in z-axis should be the same. This integral of the permeability over the porous profile area of the component is expressed by:

$$D_s(r_a^2 - r_p^2)\pi = \int_{r_p}^{r_a} D_s(r)(2\pi r)dr, \tag{2}$$

where D_s is the permeability of the material.
The dependence of the permeability on the porosity was determined experimentally in [3] for porous SiC materials. Using this relation, equation (2) can be solved regarding to r_a. For the different distributions of the porosity in the graded layer, varying thicknesses of the layer are obtained. The thicknesses of the porous layer are $6.5mm$ for the convex gradient, $7.8mm$ for the linear gradient and $14.3mm$ for the concave gradient (see Fig. 3).

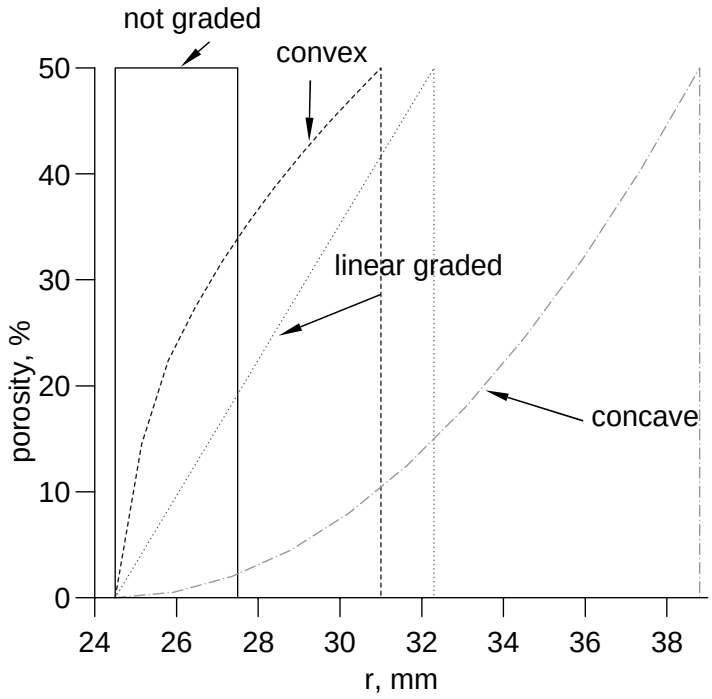

Figure 3: Porosity distributions of the porous layer.

3 Materials data

Due to its advantageous behavior at high temperature, SiC is currently used in gas turbine combustors. The material data necessary for finite element calculations (density, Young's modulus, Poisson's ratio, strength, thermal expansion

coefficient, thermal conductivity and specific heat), are based on data resulting from previous experiments [3] [6] [8]. The material data dependence of temperature and porosity are considered.

3.1 Density

The density of silicon carbide depends linearly on the porosity and is independent of the temperature:

$$\rho(P) = \rho_{P=0\%}(100 - P). \tag{3}$$

The density for 0% porosity is $\rho_{P=0\%} = 3.21 g/cm^3$

3.2 Young's modulus and Poisson's ratio

The porosity dependence of the Young's modulus can be described by a power law function [3]:

$$E(P) = E_0 e^{cP}, \tag{4}$$

with:
$E_0 = E_{P=0\%} = 455 GPa$,
$c = -0.027631$,
P is the porosity in %.
This function was obtained from several measured values for porosity and Young's modulus. Figure 4 shows the Young's modulus as a function of the porosity.
The temperature dependence of the Young's modulus is expressed by [3]:

$$E(T) = E_{T=20^oC}(1 + dT), \tag{5}$$

with:
$E_{T=20^oC} = E(P)$,
$d = -7 * 10^{-5} 1/K$.

The Poisson's ratio is assumed to be a constant $\nu = 0.159$ [3].

3.3 Strength

The Weibull parameter middle strength σ_0 of silicon carbide is assumed to be independent of the temperature [5]. The dependence of the porosity is described by:

$$\sigma_0(P) = \sigma_{0(P=0\%)} * e^{aP}, \tag{6}$$

with:
$\sigma_{0(P=0\%)} = 451.31 MPa$,
$a = -0.041495$,
Figure 5 shows the dependence of the strength on the porosity [3].

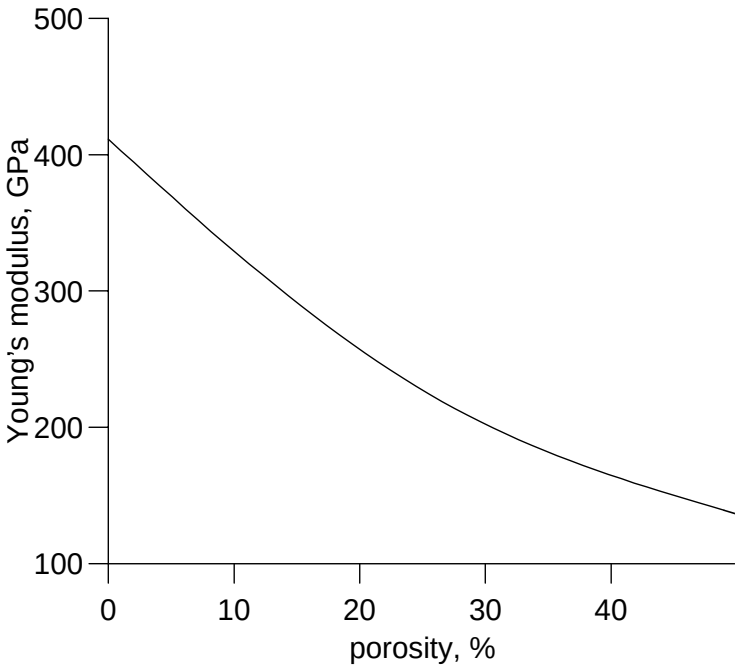

Figure 4: Young's modulus as a function of the porosity at 20^o C.

3.4 Thermal expansion coefficient

The thermal expansion coefficient is independent of porosity [6]. The temperature dependence of the thermal expansion coefficient is described by [3]:

$$\alpha(T) = c_1 + c_2 T + c_3 T^2 \tag{7}$$

with:
$c_1 = 3.59 * 10^{-6} 1/K$
$c_2 = 1.588 * 10^{-10} 1/K^2$
$c_3 = 4.44 * 10^{-15} 1/K^3$

3.5 Thermal conductivity

The porosity dependence of thermal conductivity is calculated by:

$$\lambda(P) = \lambda_{(P=0\%)}(0.4 - 0.9P) + \lambda_{(P=0\%)} \left[(0.4 - 0.9P)^2 + (0.2 - 0.2P)\right]^{1/2} \tag{8}$$

with:
$\lambda_{(P=0\%)} = \lambda(T)$

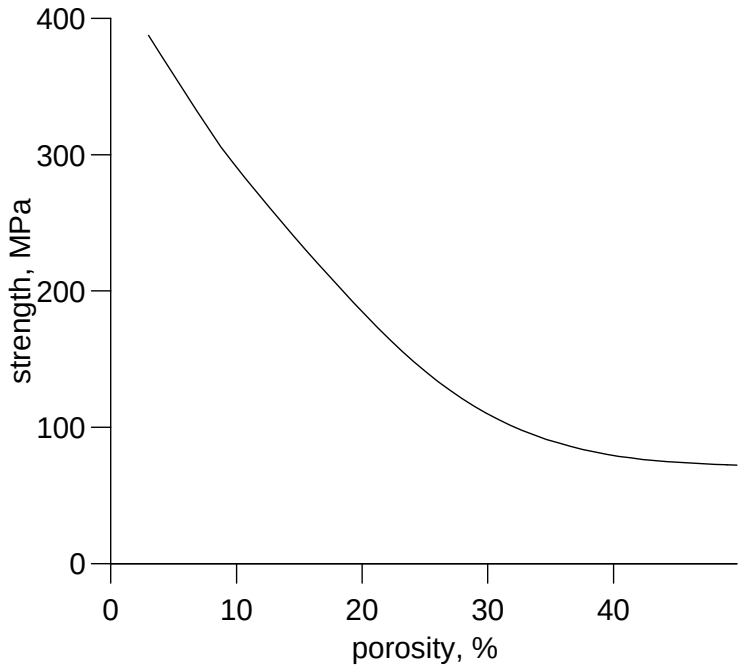

Figure 5: Strength as a function of the porosity.

Figure 6 shows the dependence of thermal conductivity on the porosity [7]. It can be seen that it is nearly a linear function.
The temperature dependence is calculated by [8]:

$$\lambda_{(P=0\%)}(T) = 100\left[c_0 + c_1 T + c_2 T^2 + c_3 T^3 + c_4 T^4 + c_5 T^5\right] \tag{9}$$

with:
$c_0 = 1.729 W/(mK)$
$c_1 = -1.982 * 10^{-3} W/(mK^2)$
$c_2 = 1.146 * 10^{-7} W/(mK^3)$
$c_3 = 1.13 * 10^{-9} W/(mK^4)$
$c_4 = -6.875 * 10^{-13} W/(mK^5)$
$c_5 = 1.252 * 10^{-16} W/(mK^6)$

3.6 Specific heat

The specific heat of silicon carbide is independent of the porosity [3]. It should be noted that the effective heat capacity of a material is dependent on the porosity. However, this influence includes the porosity dependent density.
The temperature dependence of the specific heat is calculated by [8]:

$$c_m(T) = c_0 + c_1 T + c_2 T^2 + c_3 T^3 + c_4 T^4 + c_5 T^5 \tag{10}$$

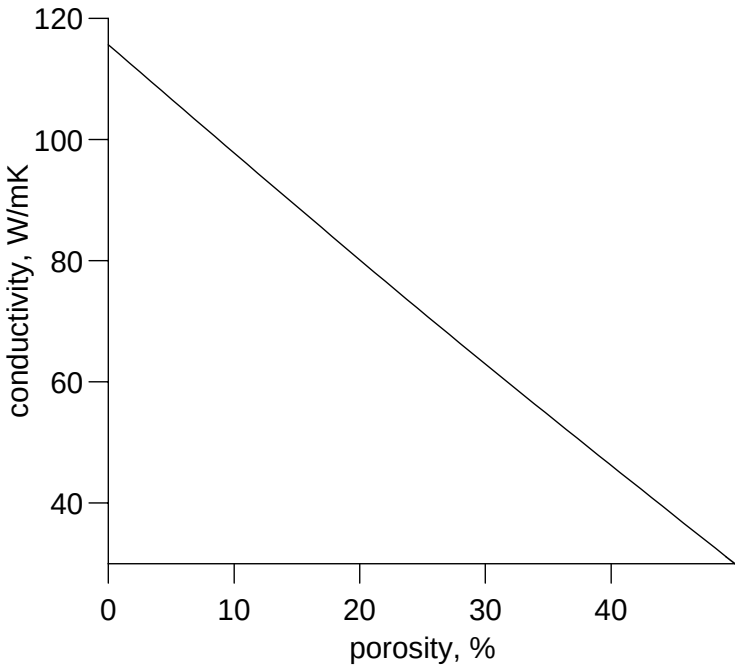

Figure 6: Thermal conductivity as a function of the porosity at 20^o C.

with:
$c_0 = -0.26596 J/(gK)$
$c_1 = 5.0197 * 10^{-3} J/(gK)$
$c_2 = -7.7423 * 10^{-6} J/(gK^3)$
$c_3 = 6.448 * 10^{-9} J/(gK^4)$
$c_4 = -2.676 * 10^{-12} J/(gK^5)$
$c_5 = 4.33 * 10^{-16} J/(gK^6)$

4 Stress boundary conditions and thermal load

Due to the thermal expansion coefficient being independent of the porosity, it is assumed that the component is stress free after its manufacturing. The component is axial symmetric and infinite in z-direction. In all directions the component is allowed to expand freely.
Thermal stresses occur due to the inhomogeneous temperature distribution, which appear both in stationary and transient modes.
It is assumed that in the beginning the component possesses a temperature of 150^oC. This accords to the temperature of the incoming compressor air. After ignition of the flame in the combustor the inner surface of the evaporator tube is heated. When the stationary mode is reached, the temperature of the inner wall is 1500^oC, the temperature of the outer wall is 550^oC.

5 Results of the stress calculations

For all four design variations (two-layers joint and the three porosity gradients) transient temperature calculations until steady state were performed and the corresponding stresses were determined. Figure 7 shows the time-dependent distribution of the stress σ_z in the non-graded model. The z-component of the stresses is chosen as an example. The maximum occurring stress in the whole component, the maximum stress in the porous material and the stress at the interface are shown. It can be seen that after about 0.6 sec. the maximum stress σ_z is in the porous material.

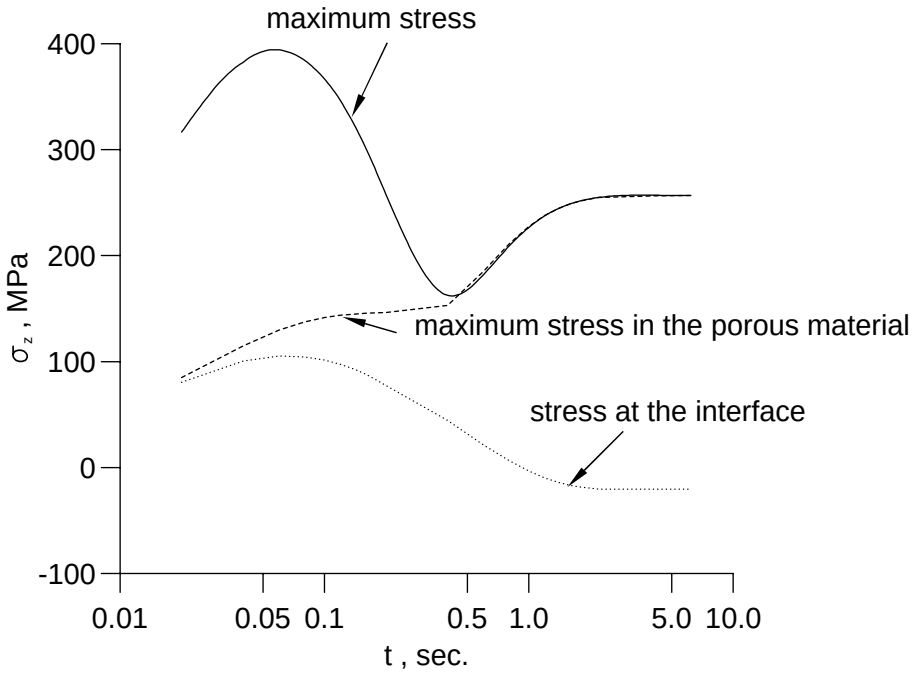

Figure 7: Stress σ_z as a function of the time for the non-graded component.

The Figures 8, 9 and 10 show the maximum stress in the porous material for the different porosity gradients.
Comparing the Figs. 7 - 10 it is obvious that the highest maximum stress σ_z is in a joint with a concave gradient, and lowest maximum stress σ_z is in the non-graded joint.
The Figures 11 - 22 show the stresses $(\sigma_r, \sigma_\phi, \sigma_z)$ along the r-axis comparing the four porosity gradients at different times. The Figures 11 - 13 show the stresses at $t = 0.02$ sec., the Figures 14 - 16 show the stresses at $t = 0.06$ sec., the Figures 17 - 19 show the stresses at $t = 0.4$ sec. and the Figures 20 - 22 show the stresses at $t = 0.22$ sec..
Comparing Figs. 11, 14, 17 and 20 it can be seen that at every time the stress σ_r for the non-graded joint is lower than that for the graded components. From

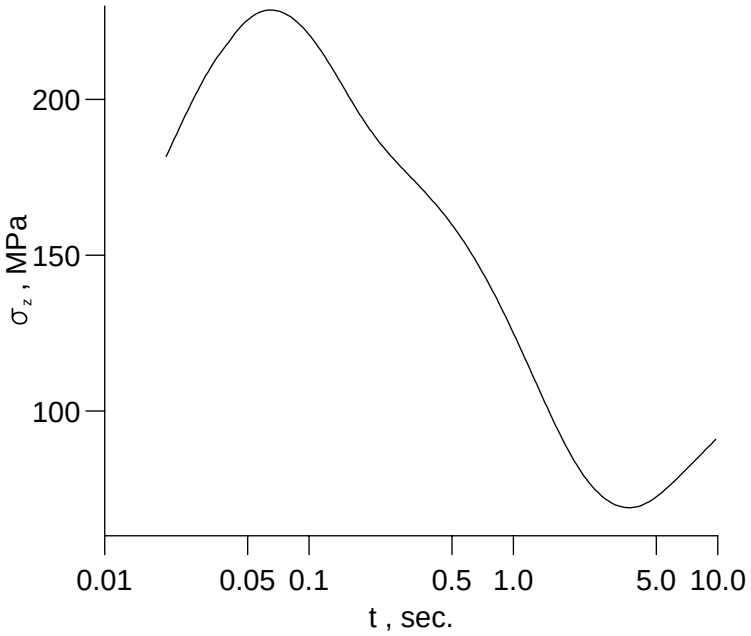

Figure 8: Maximum stress σ_z in the porous material as a function of the time for the linear porosity gradient.

Figs. 12, 15, 18 and 21 it can be seen that for the stress σ_ϕ, after about 0.4 sec. the tensile stress in the porous material for the non-graded joint is higher than that for the graded joints. For the stress σ_z this effect occurs after about 2 sec.

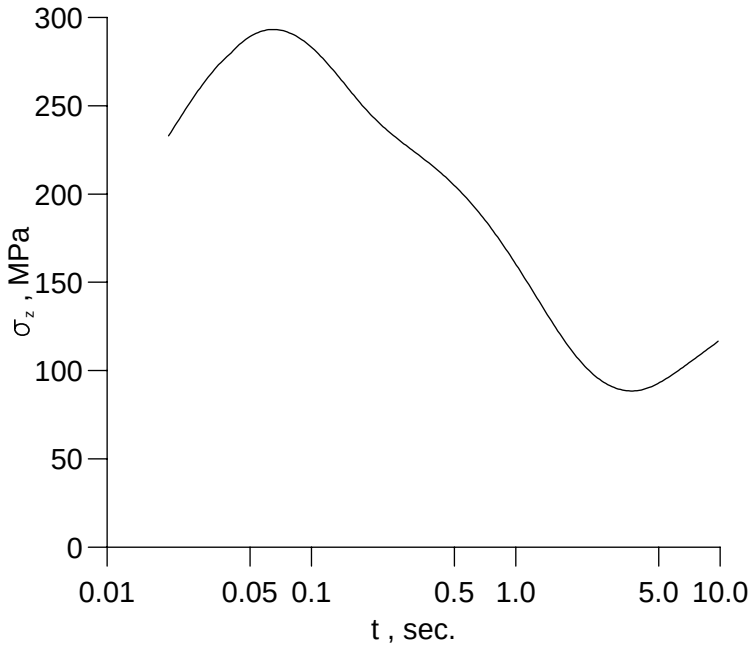

Figure 9: Maximum stress σ_z in the porous material as a function of the time for the convex porosity gradient.

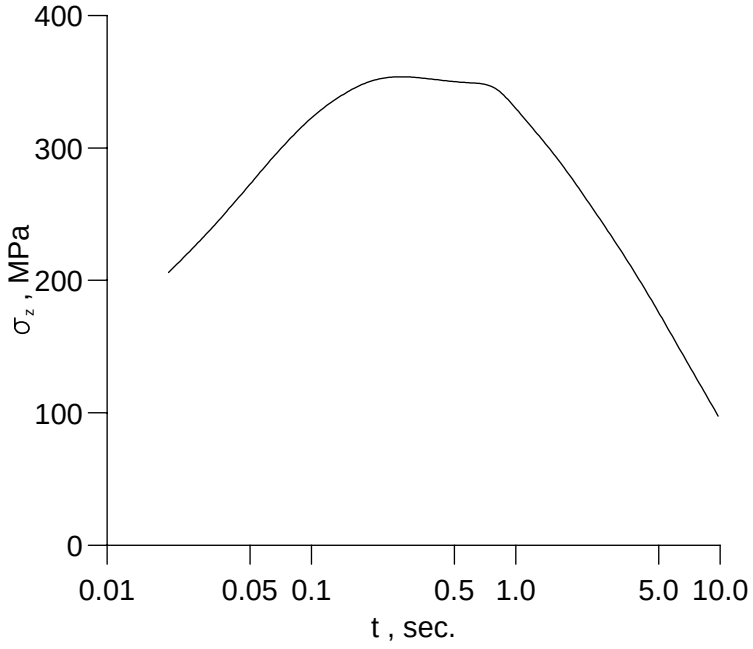

Figure 10: Maximum stress σ_z in the porous material as a function of the time for the concave porosity gradient.

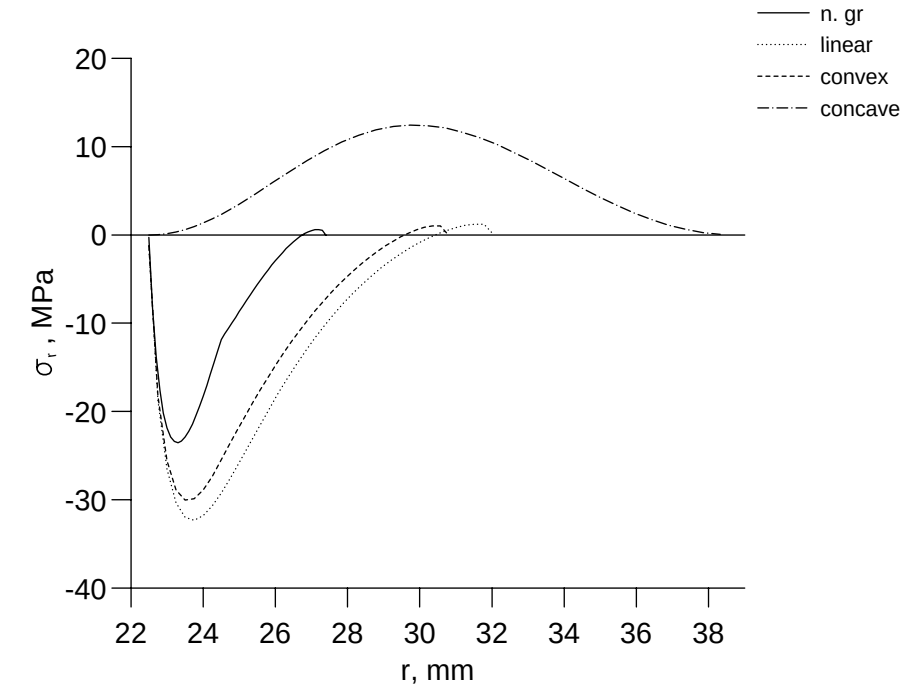

Figure 11: Stress σ_r for the four porosity gradients along the r-axis at $t = 0.02$ sec..

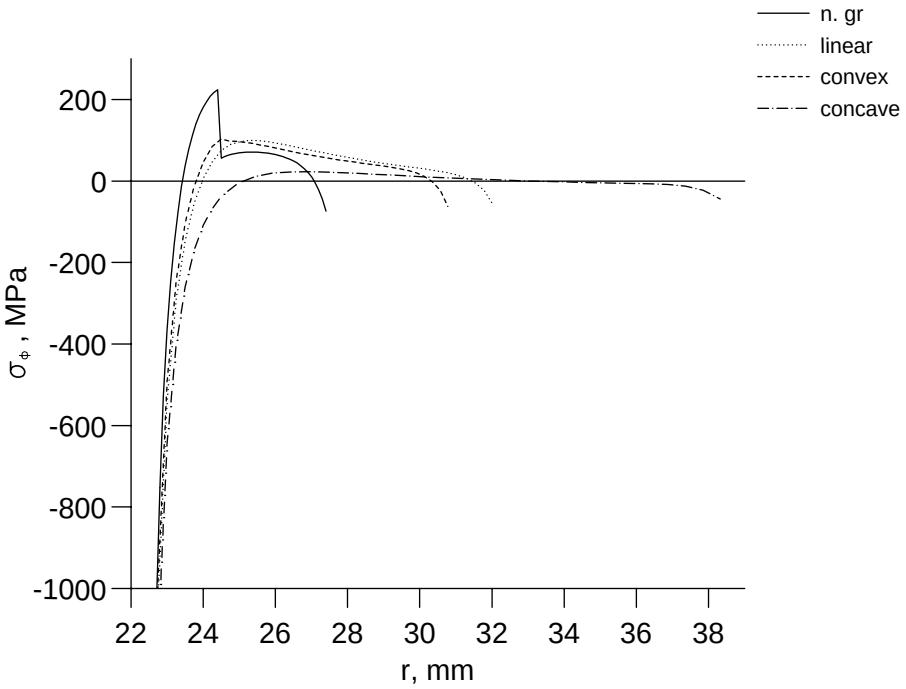

Figure 12: Stress σ_ϕ for the four porosity gradients along the r-axis at $t = 0.02$ sec..

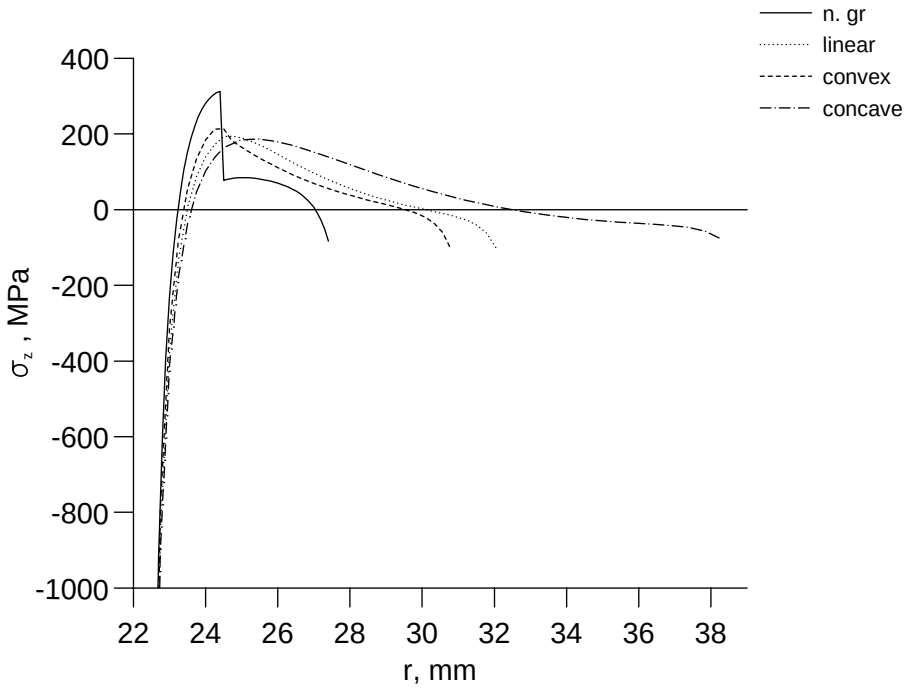

Figure 13: Stress σ_z for the four porosity gradients along the r-axis at $t = 0.02$ sec..

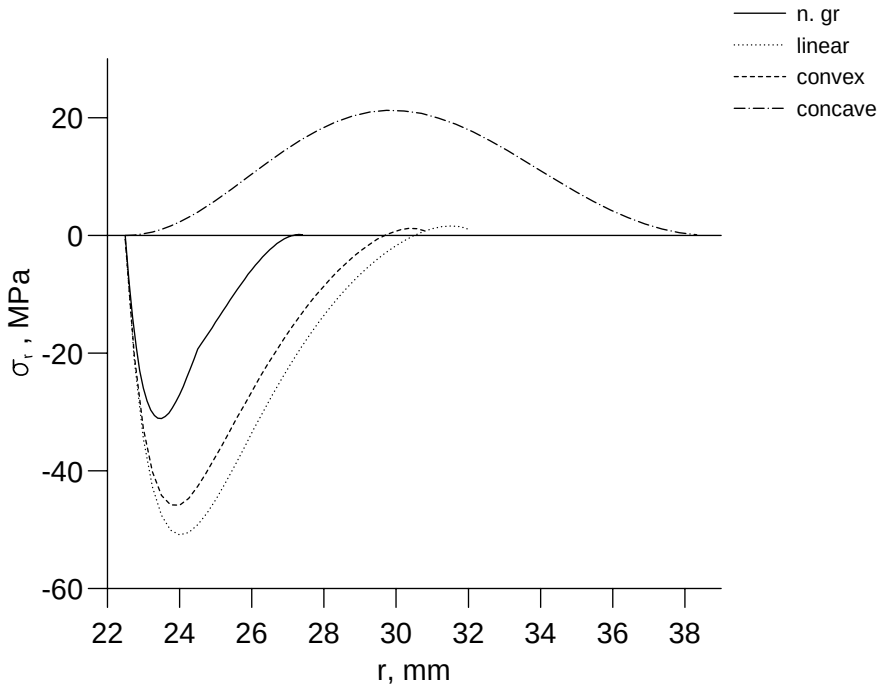

Figure 14: Stress σ_r for the four porosity gradients along the r-axis at $t = 0.06$ sec..

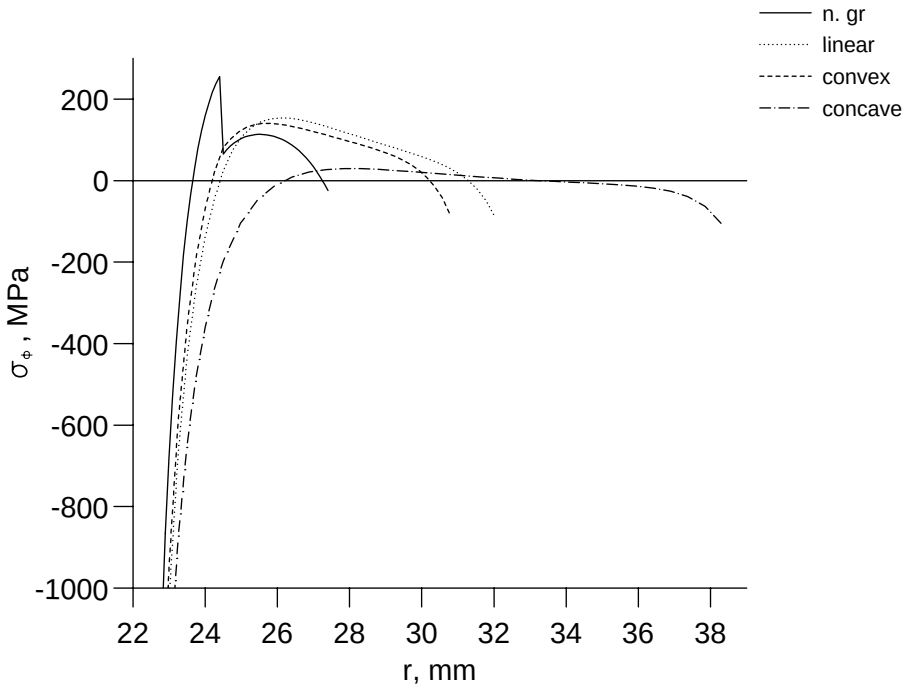

Figure 15: Stress σ_ϕ for the four porosity gradients along the r-axis at $t = 0.06$ sec..

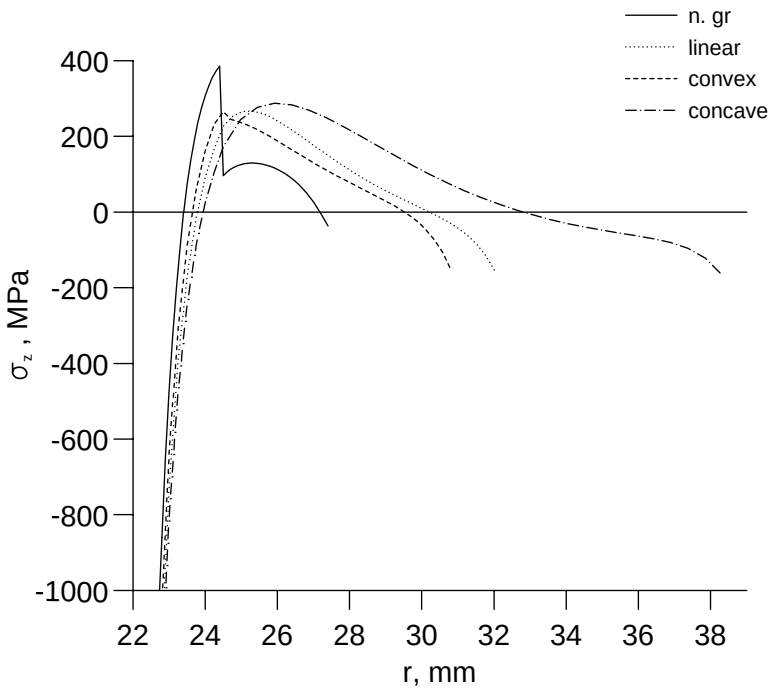

Figure 16: Stress σ_z for the four porosity gradients along the r-axis at $t = 0.06$ sec..

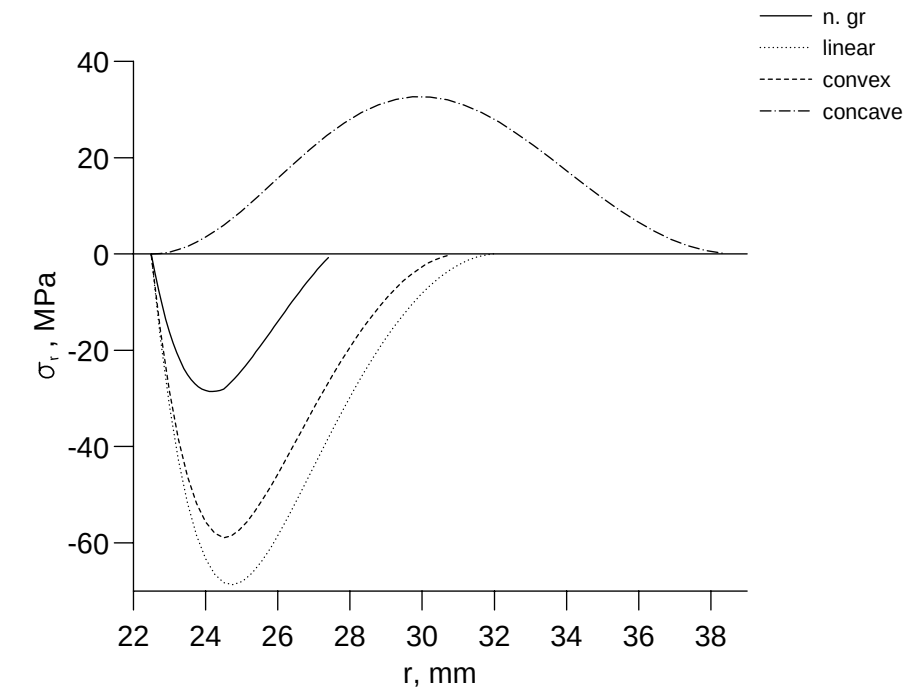

Figure 17: Stress σ_r for the four porosity gradients along the r-axis at $t = 0.4$ sec..

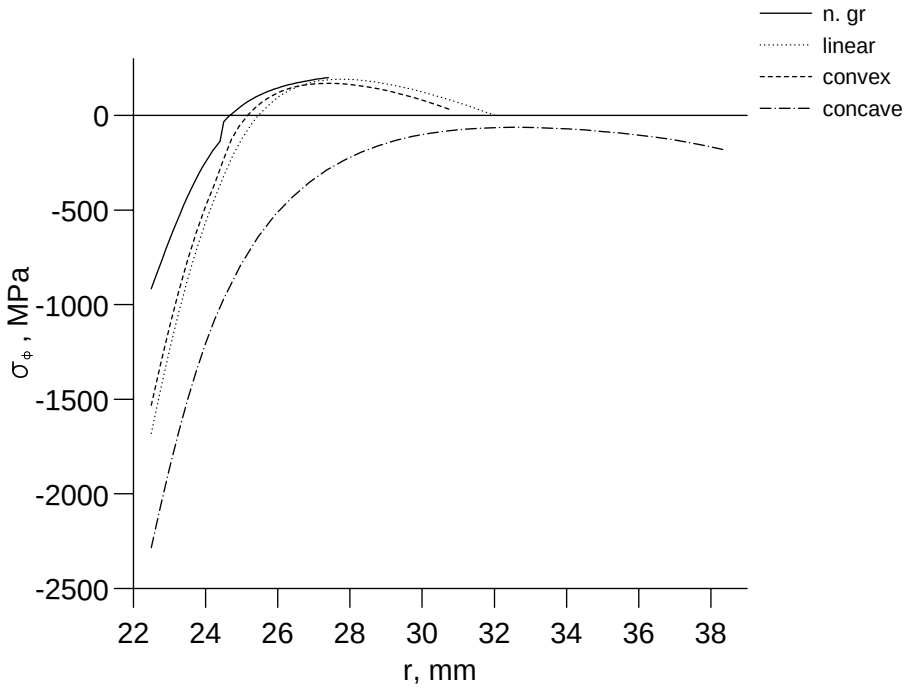

Figure 18: Stress σ_ϕ for the four porosity gradients along the r-axis at $t = 0.4$ sec..

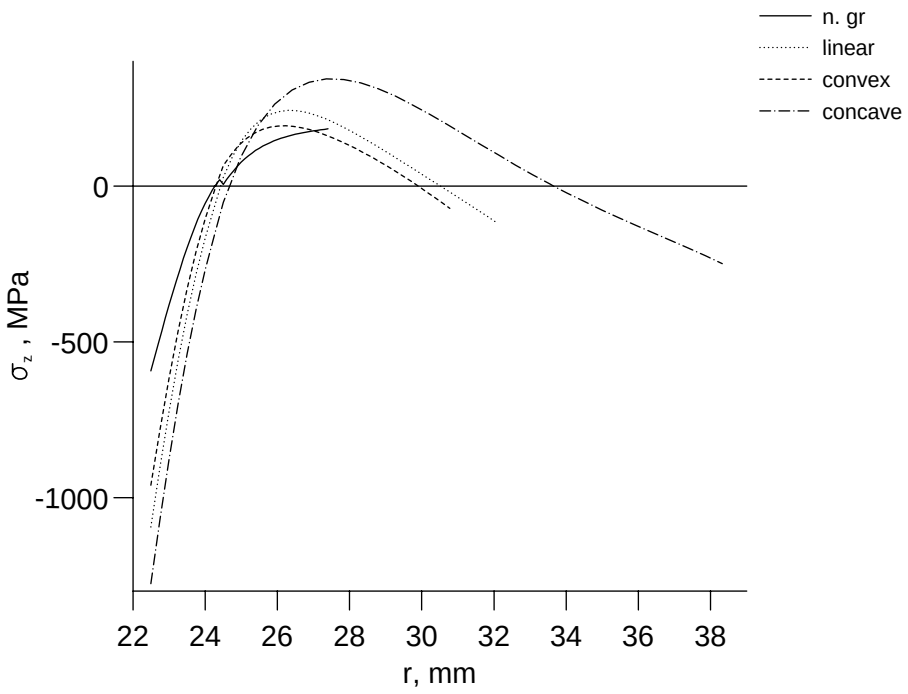

Figure 19: Stress σ_z for the four porosity gradients along the r-axis at $t = 0.4$ sec..

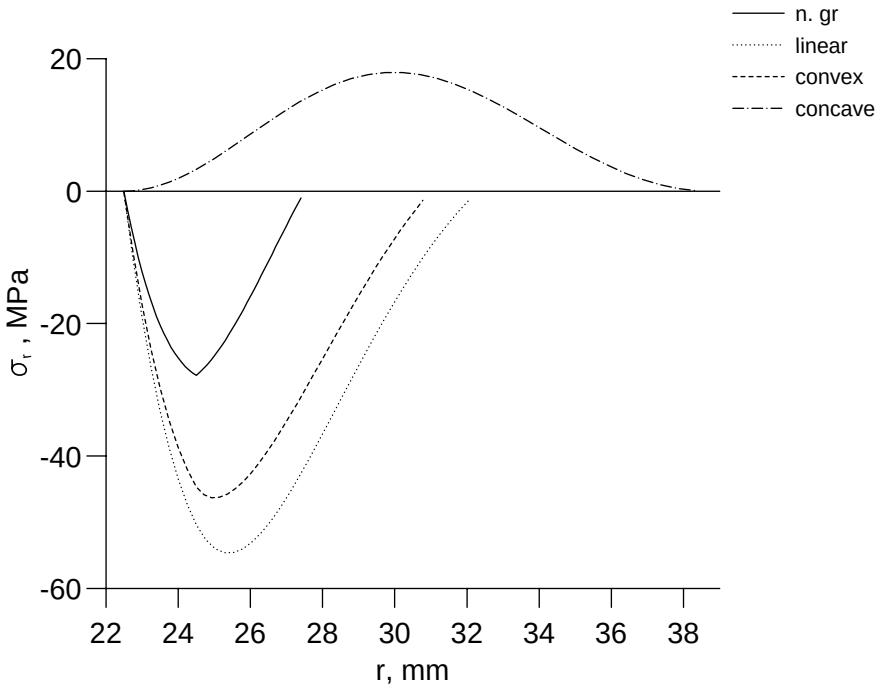

Figure 20: Stress σ_r for the four porosity gradients along the r-axis at $t = 2.2$ sec..

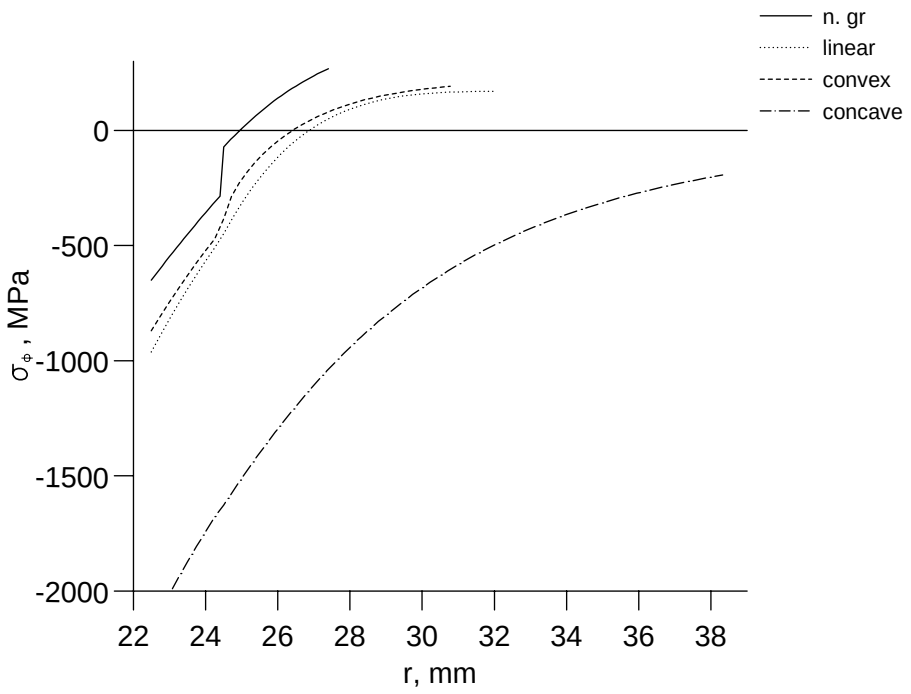

Figure 21: Stress σ_ϕ for the four porosity gradients along the r-axis at $t = 2.2$ sec..

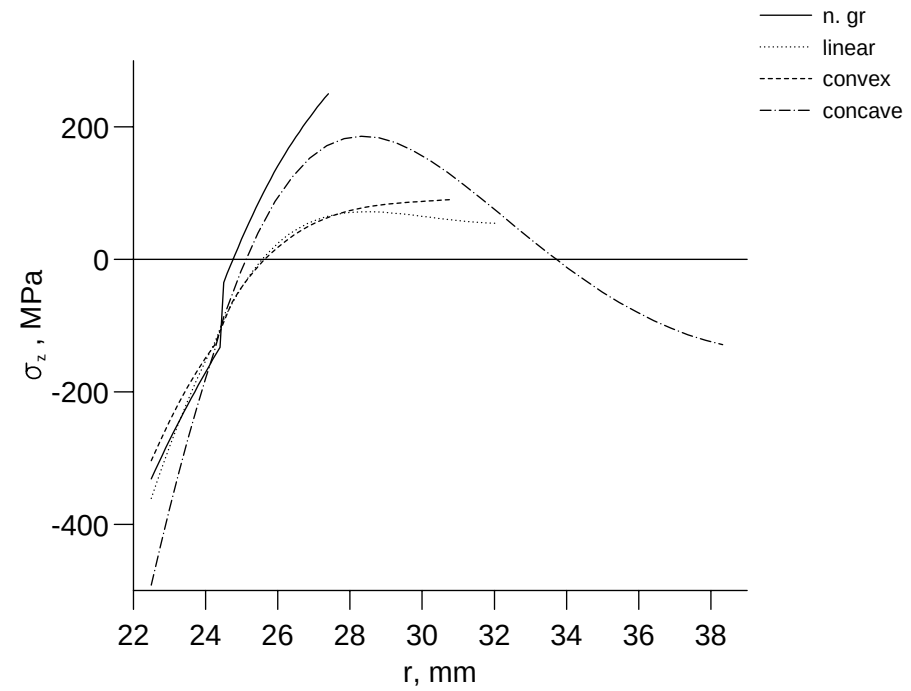

Figure 22: Stress σ_z for the four porosity gradients along the r-axis at $t = 2.2$ sec..

In Figures 23 - 29 the time dependent stresses σ_r, σ_ϕ and σ_z are shown at different positions in the component. Figure 23 compares the stress σ_r at the interface between porous and bulk material for the four porosity gradients. At this position and every time, the stress for the non-graded joint has a lower pressure than that for the linear graded joint and the convex porosity gradient. The concave porosity gradient yields tensile stresses which are more dangerous for ceramics than pressure. Figure 24 compares the stress σ_ϕ at the interface between porous and bulk material for the four porosity gradients. In this case the tensile stresses in the non-graded joint for very short times ($t < 10^{-1} sec.$) have similar values as for the linear porosity gradient. For longer times the distribution of the stresses changes to pressure. Here the non-graded joint yields significantly lower stresses than the graded joint. Figure 25 shows the stress σ_ϕ at the inner surface. The non-graded joint exhibits the lowest stresses. For the stresses σ_ϕ at the outer surface (Fig. 26) with only the concave porosity gradient pressure is obtained of all times. The Figures 27 - 29 show the corresponding distributions for σ_z. Here also, advantages for the application of the graded joint are only found at the outer surface.

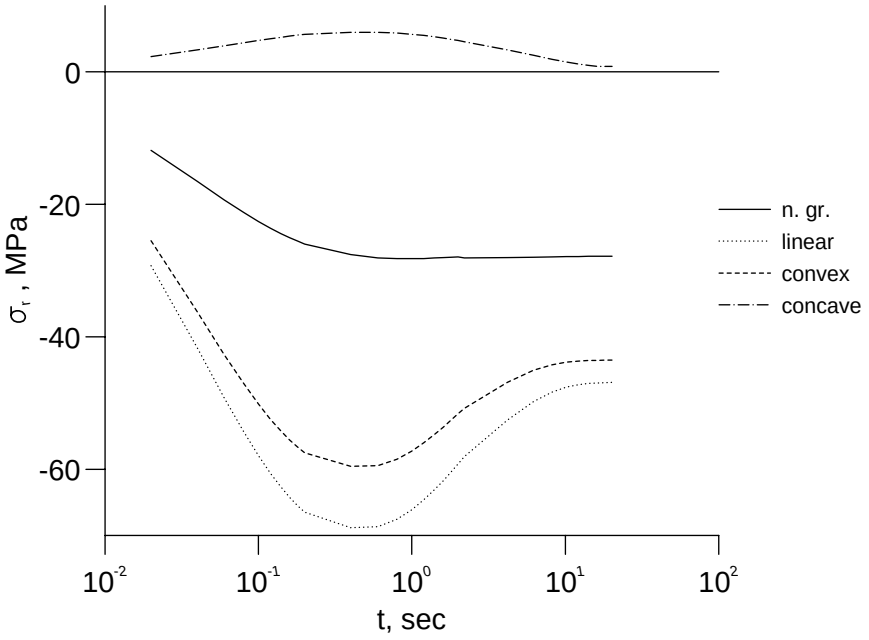

Figure 23: Stress σ_r at the interface as a function of the time for the four porosity gradients.

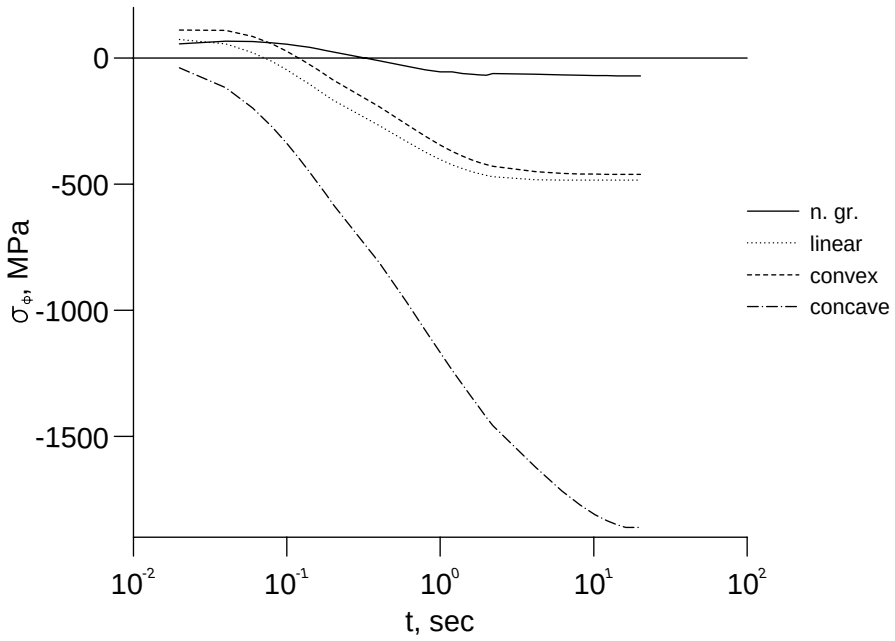

Figure 24: Stress σ_ϕ at the interface as a function of the time for the four porosity gradients.

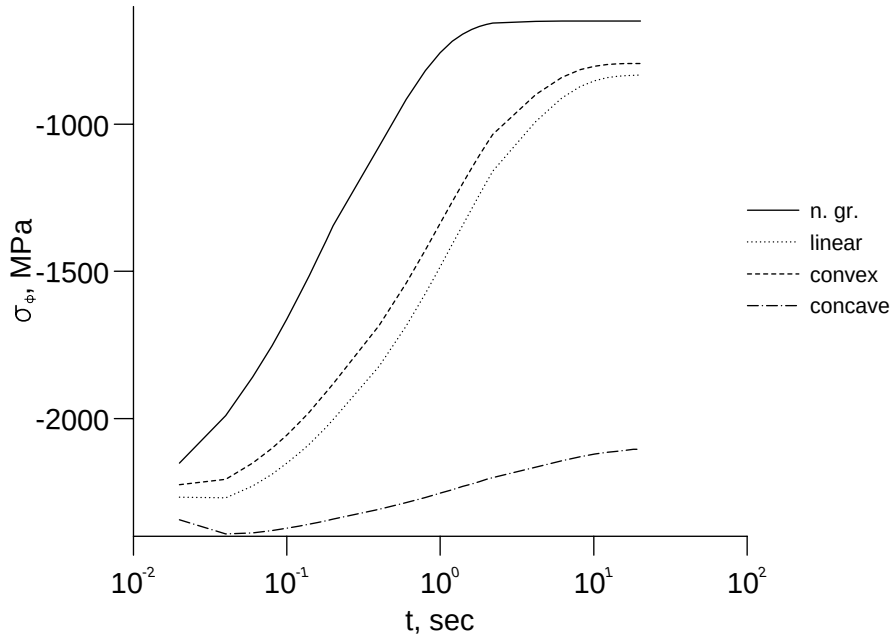

Figure 25: Stress σ_ϕ at the inner surface as a function of the time for the four porosity gradients.

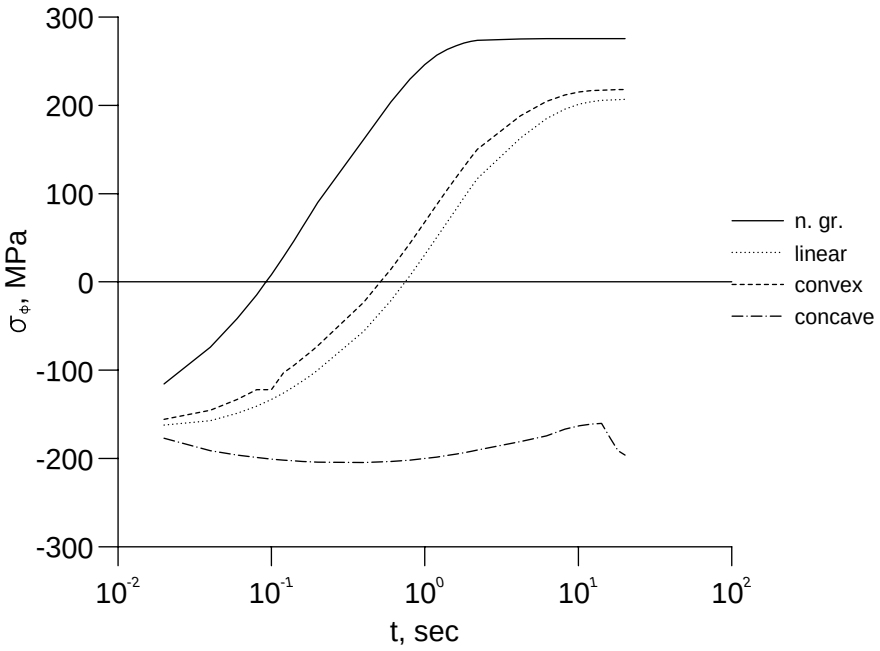

Figure 26: Stress σ_ϕ at the outer surface for the four porosity gradients, as a function of the time.

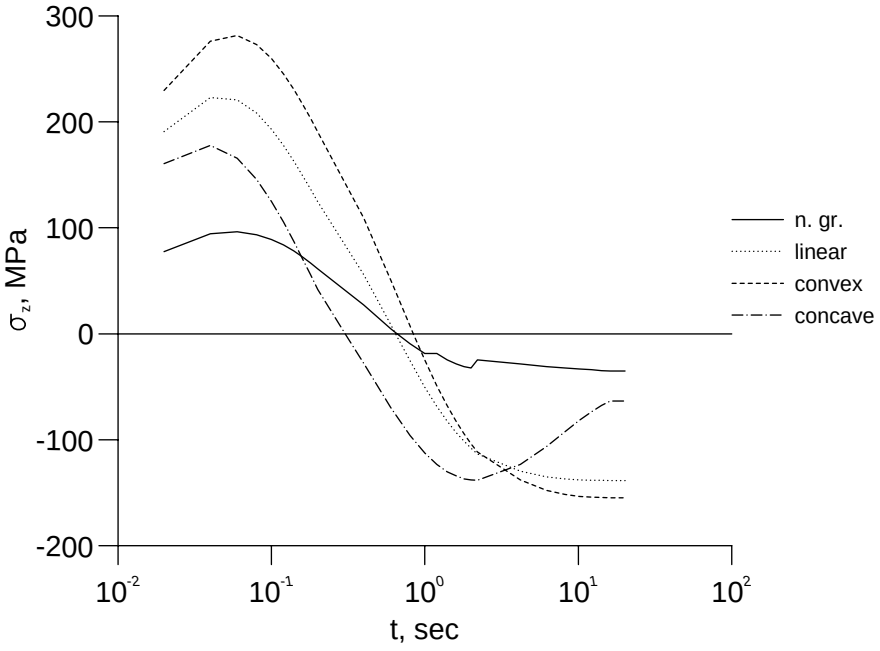

Figure 27: Stress σ_z at the interface as a function of the time for the four porosity gradients.

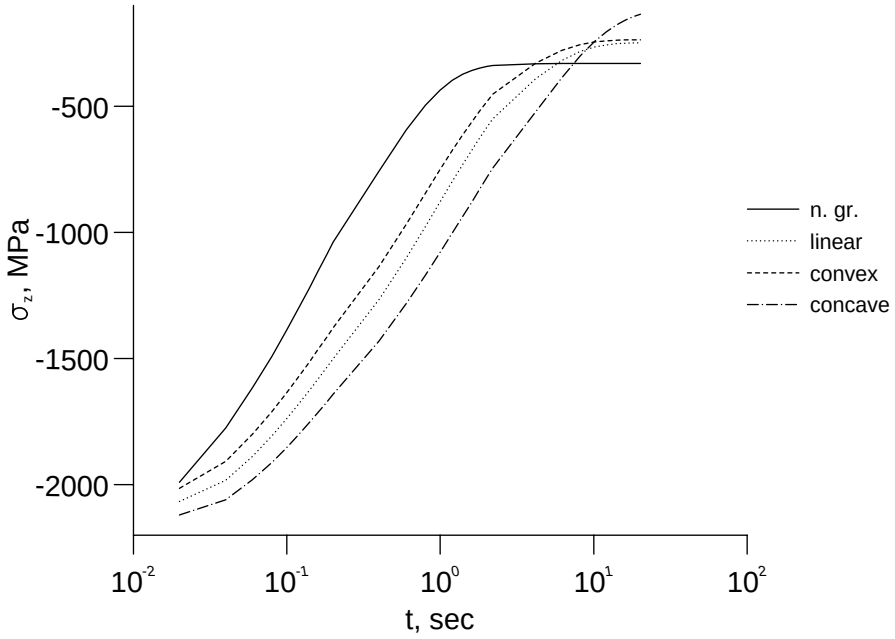

Figure 28: Stress σ_z at the inner surface as a function of the time for the four porosity gradients.

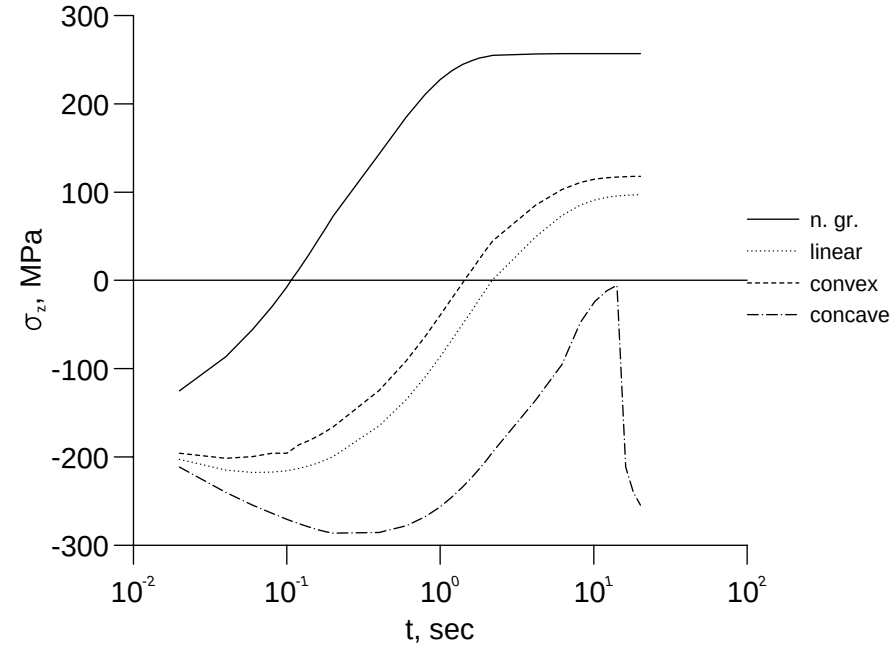

Figure 29: Stress σ_z at the outer surface as a function of the time for the four porosity gradients.

Comparing the results shown in Figures 7 - 29, it can be seen that for this component the stresses in z - and ϕ-direction are similar for a short time and always higher than the stresses in r-direction.
Therefore in the following, only the stresses in z - direction are considered.
In Figures 30 - 33 the maximum tensile stress σ_z for every point along the r-axis is shown for all time, which appears during the heating process. The stresses are compared with the local strength, given in [3]. These strengths are porosity-dependent Weibull parameters σ_0. These values were determined from homogenious porous SiC speciments with ring-on-ring tests.
In the two-layers joint, the stresses σ_z in the porous layer are higher than the strength both in steady state and transient mode (see Fig. 30). The component contains a high probability of failure in the beginning of the first heating process.

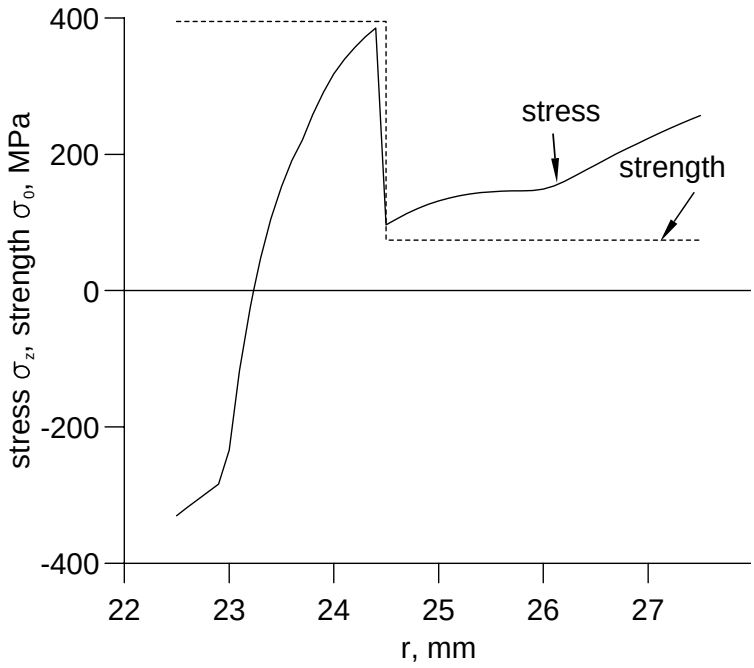

Figure 30: Two-layer joint: Comparison of the local stresses σ_z and strength σ_0 along the r-axis.

During heating pressure stress occurs at the inner surface in the components in all design variants with a graded porous layer. Along the r-axis there is a maximum of tensile stress nearly in the middle of the porous layer. Concerning the convex (see Fig. 32) and the linear porosity gradient (see Fig. 31) this maximum exceeds the local strength σ_0 of the material, so the failure probability of the component is very high. In steady state, tensile stresses are found at the outer surface of the evaporator tube. A significant maximum is not found along the r-axis. The

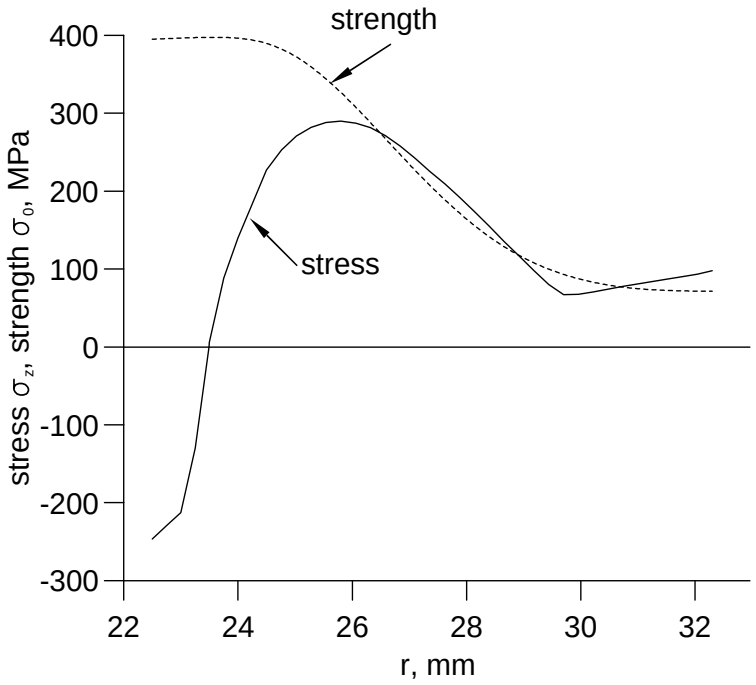

Figure 31: Linear porosity gradient: Comparison of the local stresses σ_z and strength σ_0 along the r-axis.

tensile stress at the outer surface will also lead to failure for the linear and the convex gradients.
Finite element calculations have shown that it is possible to always keep the stresses lower than the local strength σ_0, by using only the concave porosity gradient (see Fig. 33). Due to the boundary condition of constant flow resistance of the porous layer, the graded layers are thicker than the non-graded layer.
In the next section, the effect of the thickness of the porous layer will be examined.

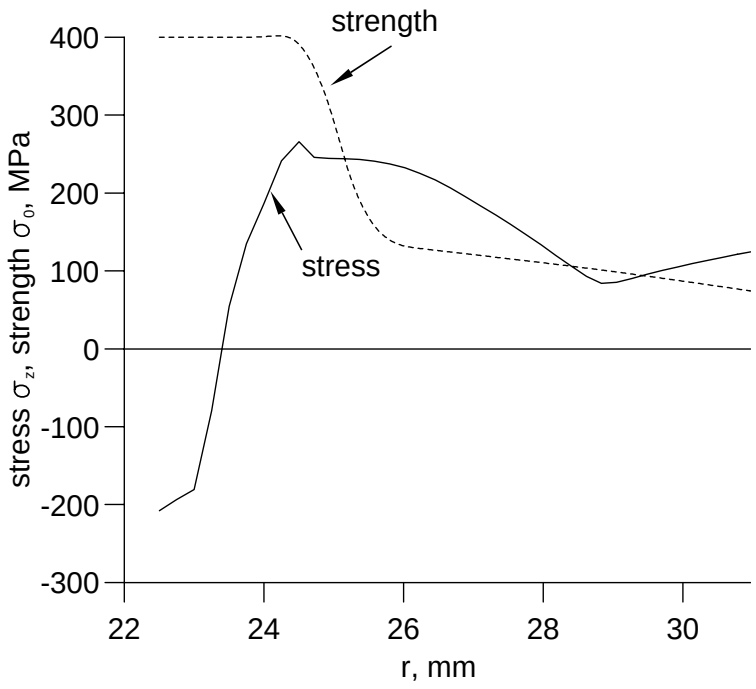

Figure 32: Convex porosity gradient: Comparison of the local stresses σ_z and strength σ_0.

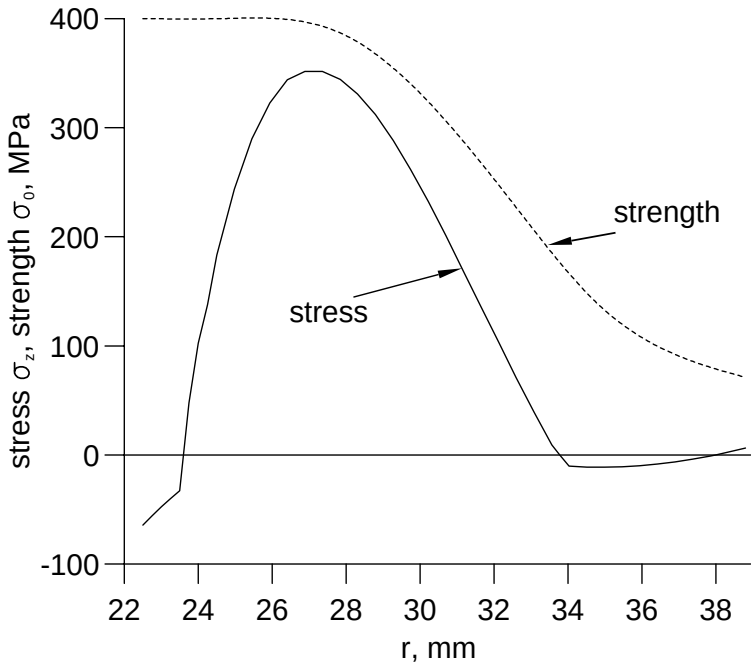

Figure 33: Concave porosity gradient: Comparison of local stresses σ_z and strength σ_0.

6 Effect of the transition function on the stresses for a constant layer thickness

It could be possible that the lower failure probability of the graded components, as shown in the previous section, is induced by the greater thickness of the different graded layers. This fact shall be proven by comparing different designs with a constant layer thickness and a constant surface porosity of 50% . The thickness of the graded layer is constant $14.3mm$, i.e. the thickness of the layer for the concave function. With this thickness the stream resistance of the two-layer system, the linear and the convex graded model is smaller than necessary. This fact will not disturb the function of the device. Figs. 34 - 36 show the distribution of the stress σ_z for the two-layer joint, the convex and the linear porosity gradients.

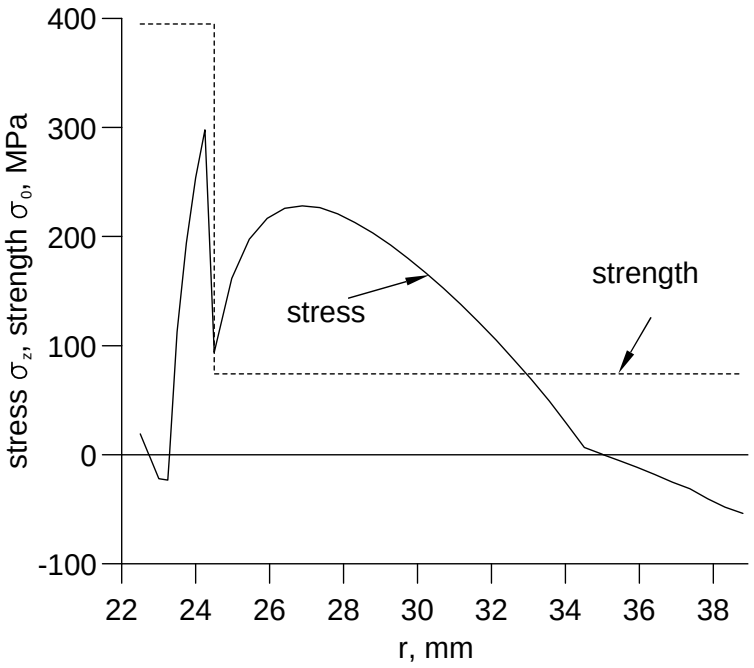

Figure 34: Two-layer joint (porous layer thickness $14.3mm$): Comparison of local stresses σ_z and strength σ_0 along the r-axis.

The stresses are again shown for the maximum stresses which occur at each point on the r-axis during the transient heating of the component. It can be seen that also for this additional geometrical boundary condition, the stress σ_z of the two-layer joint, the convex and linear porosity gradients are higher than the local strength σ_0.

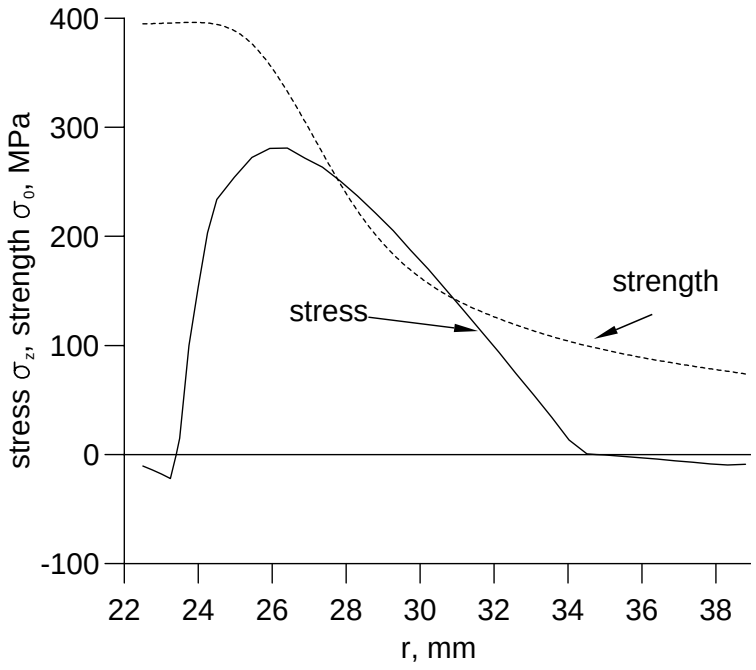

Figure 35: Linear porosity gradient (porous layer thickness $14.3mm$): Comparison of the local stresses σ_z and strength σ_0 along the r-axis.

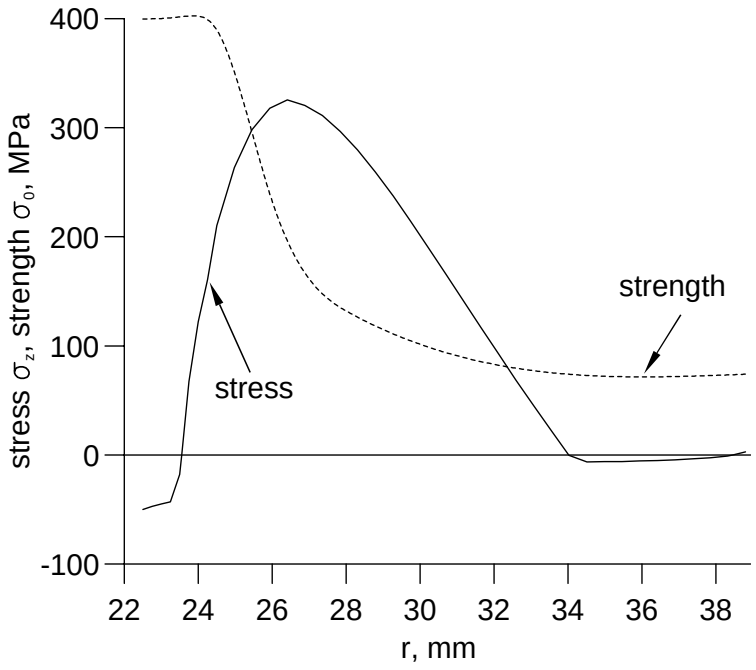

Figure 36: Convex porosity gradient (porous layer thickness $14.3mm$): Comparison of the local stresses σ_z and strength σ_0 along the r-axis.

In the above examples, it was assumed that every design variation has the same layer thickness and surface porosity. With these two conditions the global permeability of the components is greater than necessary for the two-layers joint, the linear porosity gradient and the convex porosity gradient. Another possibility would be to reduce the surface porosity for these three functions to obtain a constant permeability for the constant thickness. With this condition, a surface porosity of 27.7% for the two-layers joint is obtained, for the linear porosity gradient we get a surface porosity of 42.0% and for the convex porosity gradient 36.2%. In this case the strength of the material in the porous layer is much higher than that shown in the above example.
The stresses were calculated in the same way as for the previous examples, the results are shown in the Figures 37 - 39. It can also be seen that for this geometrical boundary condition only the stress σ_z of the concave porosity gradient is lower than the local strength.

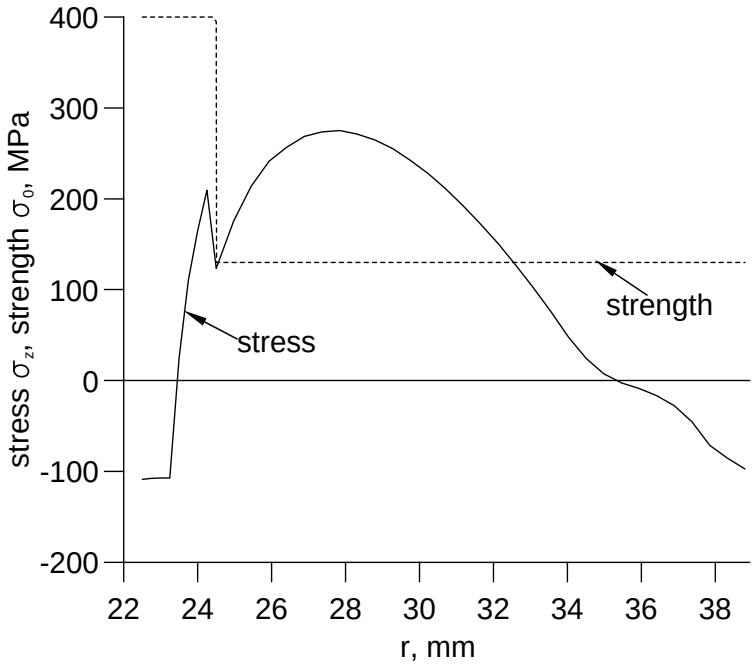

Figure 37: Two-layer joint (porosity at the surface = 27.7%): Comparison of the local stresses σ_z and strength σ_0 along the r-axis.

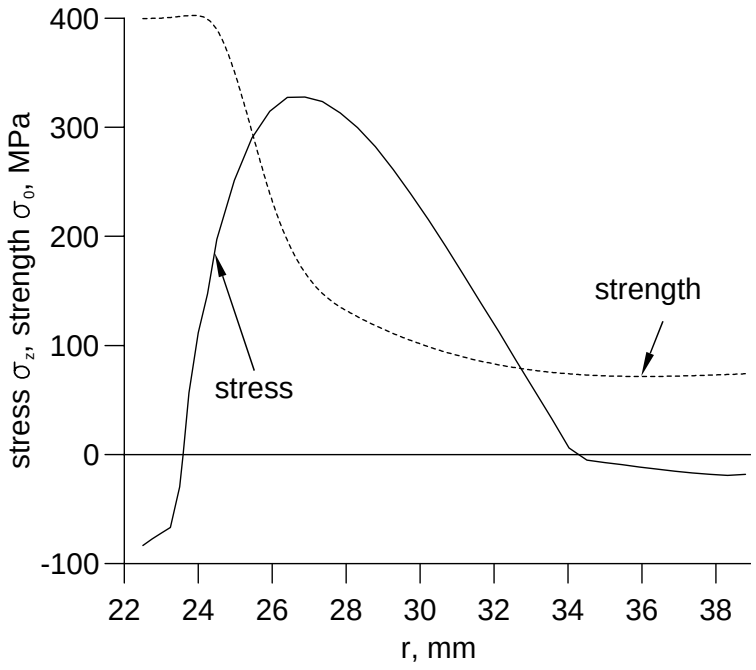

Figure 38: Linear porosity gradient (porosity at the surface = 42.0%): Comparison of the local stresses σ_z and strength σ_0 along the r-axis.

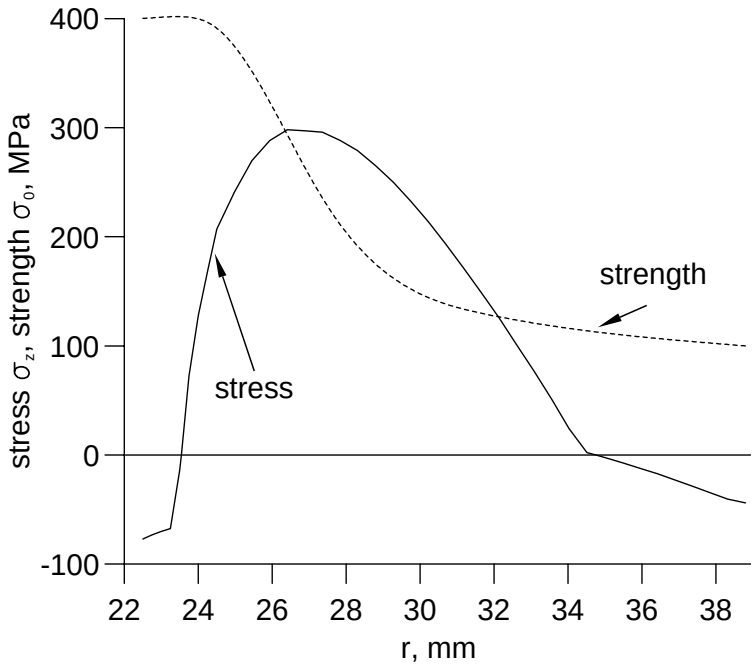

Figure 39: Convex porosity gradient (porosity at the surface = 36.2%): Comparison of the local stresses σ_z and strength σ_0 along the r-axis.

7 Calculation of the failure probability in a joint using FGM

For the regarded components a calculation of the failure probability is based on the Weibull theory. The failure probability can be calculated from:

$$P_f = 1 - exp\left[-\frac{1}{V_0}\frac{1}{4\pi}\int_V\int_\Omega\left(\frac{\sigma_{eq}}{\sigma_0}\right)^m d\Omega dV\right], \tag{11}$$

where:
P_f = global failure probability for volume failures,
Ω = surface of the unit sphere,
V_0 = volume of the component,
m, σ_0 = Weibull parameter,
σ_{eq} = equivalent stress.
For the Weibull parameter strength σ_0, its values were known as a function of the porosity as shown in the former section. The Weibull parameter m is independent of the porosity and $m = 8.5$ [3].
The calculations using the thermal load, geometries and strengths given in the former sections led to a failure probability of 1 for all design variants. It can be shown that the concave porosity gradient yields better results.
To turn out the advantages of the optimized transition function for the failure probability, the values of the failure probability should be smaller than 1. This can be reached by reducing the thermal load and by increasing the strength of the material, i.e.

- the temperature gradient in the component is reduced by increasing the temperature at the outer surface of the evaporator tube to 750^o C and by reducing the temperature at the inner surface to 1200^o C,
- a thickness of the inner solid layer of 4mm is chosen to reduce the temperature gradient,
- the Weibull parameter σ_0 is doubled and m = 20 is used.

With these values and boundary conditions the time-dependent failure probability is calculated. It is assumed that the component is heated until steady state is reached. In the stress calculations, it was assumed that the length of the component is infinite. However, failure probability depends on the volume of the component. For the calculation of the failure probability a length of one millimeter is chosen.
For the first design variant a failure probability of $P_f = 0.156$ is obtained for the non-graded component, for the convex porosity gradient $P_f = 6.29 * 10^{-4}$, for the linear porosity gradient $P_f = 4.39 * 10^{-6}$ and for the concave porosity gradient $P_f = 1.80 * 10^{-7}$. The great advantage for the concave porosity gradient also

appears for the calculation of the failure probability.
The failure probability is also calculated for the second design variant with a constant layer thickness of $14.3mm$ (see section 7). Assuming a constant surface porosity of 50%, a failure probability of $P_f = 0.185$ for the non-graded component is obtained. For the linear porosity gradient $P_f = 1.54 * 10^{-5}$, and for the convex porosity gradient $P_f = 6.79 * 10^{-3}$.
For the third design variant, the assumption of a fitted surface porosity with a constant thickness and a constant permeability for the four porosity gradients, a failure probability of $P_f = 0.994 * 10^{-2}$ for the non-graded component is obtained, for the linear porosity gradient $P_f = 8.34 * 10^{-6}$, and for the convex porosity gradient $P_f = 3.60 * 10^{-4}$. It should be noted, that the failure probability for the concave porosity gradient is constant for these design variations.
The failure probabilities for different design variants are shown in Fig. 40. It is obvious that the concave transition function is the best in terms of failure probability.

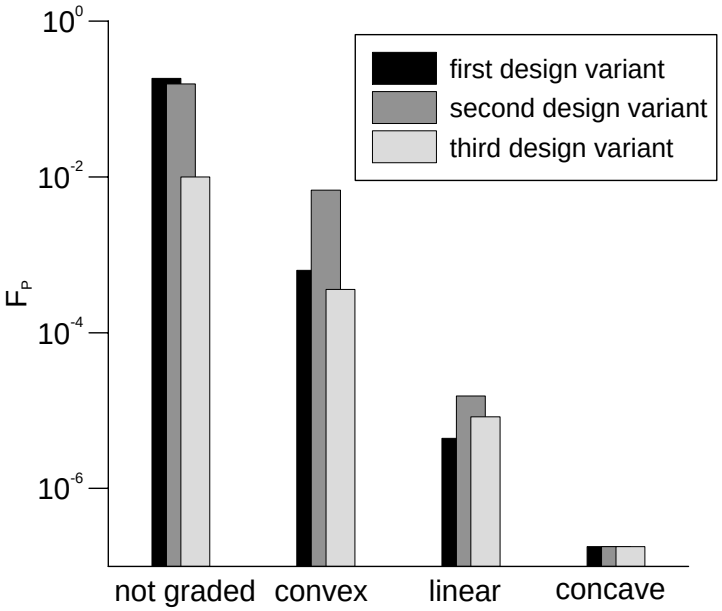

Figure 40: Comparison of failure probability for the different design variants.

8 Conclusions

The stress calculations have shown that in some cases the non-graded joint is better than a joint with functionally graded materials. From the failure probability calculations it is obvious that a joint with functionally graded materials, especially with a concave transition function, is much more advantageous than a non-graded joint. The concave gradient of the porosity has the best relation between stresses and local strength at any time. With the calculations made until now, it could be shown that the failure probability of this component can be reduced significantly by using a tailored gradient. For further optimization it would therefore be necessary to consider three-dimensional components with a real length and boundary effects at the end of the tube.
Along with this theoretical work, a processing route has been developed, which is able to produce such tailored porosity gradients [9].

The financial support of the Deutsche Forschungsgemeinschaft is gratefully acknowledged.

References

[1] Pfeiffer A.
Entwicklung einer keramischen Kleingasturbinen-Brennkammer: Neue Möglichkeiten zur schadstoffarmen Verbrennung, Doctoral thesis, Universität Karlsruhe (TH), 1992

[2] Brandauer M., Schulz A., Wittig S.
Optimierung der Filmverdampfung auf porösen keramischen Oberflächen zur NO_x- armen Verbrennung, Sonderforschungsbereich 167, Forschungsbericht 1993-1994-1995, pp. 373-388, Universität Karlsruhe (TH), 1995

[3] Dröschel M.
Grundlegende Untersuchung zur Eignung poröser Keramiken als Verdampferbauteile, Doctoral thesis, Universität Karlsruhe (TH), IKM 022, ISSN 1436-3488, 1998

[4] Brandauer M., Schulz A., Wittig S.
Optimierung der Filmverdampfung auf porösen keramischen Oberflächen zur NO_x-armen Verbrennung, Sonderforschungsbereich 167, Forschungsbericht 1993-1994-1995, pp. 373-388, Universität Karlsruhe (TH), 1995

[5] Münz, S.
Entwicklung und maschinentechnische Bewertung neuer konstruktiver Konzepte für ein keramisches Flammrohr, Doctoral thesis, Universität Karlsruhe (TH), 1995

[6] Ondracek, G.
Zum Zusammenhang zwischen Eigenschaften und Gefügestruktur mehrphasiger Werkstoffe, Bericht des Kernforschungszentrums Karlsruhe, KfK 5371, August 1978

[7] Schulz, B.
Thermal conductivity of porous and highly porous materials, High temperature, high pressures, Vol. 13, pp. 649-660, 1981

[8] Zimmermann, H.
Thermoschock- und Thermowechselverhalten verschiedener keramischer Materialien, Bericht des Kernforschungszentrums Karlsruhe, KfK 5303, April 1994

[9] Dröschel, M., Oberacker, R., Hoffmann, M.J.
Simulation of pressure filtration process for making porosity graded silicon carbide evaporator tubes, to be published in the Proceedings of the 5th International Symposium on Functionally Graded Materials (FGM 98), Dresden, 26.-29.10.1998